Catalysis Science & Technology

PAPER

View Article Online
View Journal | View Issue

Cite this: *Catal. Sci. Technol.*, 2017, 7, 3151

Influence of pore topology on synthesis and reactivity of Sn-modified zeolite catalysts for carbohydrate conversions†

William N. P. van der Graaff,[a] Christiaan H. L. Tempelman,[a] Evgeny A. Pidko *[abc] and Emiel J. M. Hensen *[a]

A range of Sn-modified MWW, MFI, MOR and Beta zeolites were prepared by a post-synthetic Sn functionalization method and their catalytic properties for sugar conversions were evaluated. The focus of this work was to understand the effect of micropore dimensions and additional mesoporosity on the Sn incorporation and on the catalytic properties. The post-synthetic approach, which involves acid-dealumination of the parent zeolite followed by $SnCl_4$ grafting, is highly efficient for the selective incorporation of lattice Sn sites in wide-pore Beta and MOR zeolites. The modification of the medium-pore MWW and MFI is impaired by the more difficult dealumination and hence the lower efficiency of the Sn incorporation. Hierarchical structuring of the zeolites allows the increase of the Sn loading in the final zeolites. The catalytic properties were assessed in the isomerization and retro-aldolization reactions of glucose and the conversion of 1,3-dihydroxyacetone to methyl lactate. The catalytic results depend strongly on the structural and topological properties of the catalysts as well as on the reactant. Glucose isomerization carried out at a relatively low temperature is mainly limited by strong adsorption of carbohydrates to the active sites. This explains why zeolite nanostructuring had little effect on the catalyst activity, which instead depends mainly on the zeolite topology and the nature of the reactive Sn centers. The influence of pore size is most pronounced for Sn-MWW and Sn-MFI zeolites which are inactive in glucose-to-fructose isomerization, but perform in the higher-temperature retro-aldolization of carbohydrates with an activity similar to that of Sn-Beta. Because of the limited accessibility of the Sn sites inside the 1D MOR pore system, Sn-MOR catalysts were only moderately active in all probe reactions considered.

Received 24th May 2017,
Accepted 12th June 2017

DOI: 10.1039/c7cy01052d

rsc.li/catalysis

1. Introduction

The development of a more sustainable and green chemical industry requires new chemical processes for the production of useful chemicals from renewable feedstock. In this respect, cellulosic biomass is an attractive alternative to fossil resources as it is an abundant and renewable source of carbon for the production of platform chemicals with a wide range of possible down-stream applications. Most of the conversion paths (Fig. 1) discussed so far involve the sequential depolymerization of cellulose using acid catalysis followed by the conversion of glucose monosaccharide to value-added chemicals such as 5-hydroxymethylfurfural (HMF) or lactic acid derivatives (*e.g.* lactic acid (LA) and methyl lactate (ML)).[1,2]

The isomerization of glucose to its more reactive isomer fructose is one of the most important steps in the overall conversion to these platform chemicals (Fig. 1).[3–6] This reaction

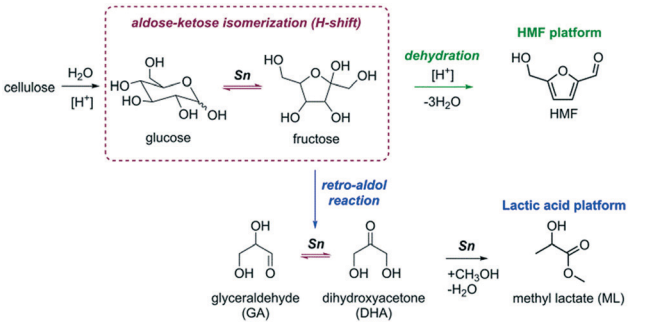

Fig. 1 Reaction pathways for the catalytic conversion of cellulose into the renewable chemical platform molecules 5-hydroxymethylfurfural (HMF) and lactic acid. The role of Lewis acid Sn and Brønsted acid sites is indicated.

[a] *Inorganic Materials Chemistry Group, Schuit Institute of Catalysis, Eindhoven University of Technology, PO Box 513, 5600 MB Eindhoven, The Netherlands. E-mail: e.a.pidko@tue.nl, e.j.m.hensen@tue.nl*
[b] *Institute for Complex Molecular Systems, Eindhoven University of Technology, PO Box 513, 5600 MB Eindhoven, The Netherlands*
[c] *ITMO University, Lomonosova str. 9, 199034 St. Petersburg, Russia*

† Electronic supplementary information (ESI) available: Supplementary catalytic results and characterization data. See DOI: 10.1039/c7cy01052d

is catalyzed by Lewis acids, and the most studied catalyst is Sn-Beta zeolite.[7,8] The unique activity of Sn-Beta zeolite for the isomerization and retro-aldolization of carbohydrates (Fig. 1) stems from the strong Lewis acid Sn sites embedded in the framework of Beta zeolite.[9] Other zeolites modified with Sn have also been considered for sugar conversions.[10–14] Sn (and Ti)-modified MFI zeolites, which have narrower pores than Beta zeolite, were found to be inactive for glucose isomerization.[9,12] Although the glucose isomerization activity of Sn-modified MWW zeolite was very low,[11] this catalyst was highly active for the retro-aldolization of sugars to methyl lactate in methanol. Other Sn-containing materials such as amorphous silica with an ordered mesoporous structure such as Sn-SBA-15 and Sn-MCM-41 can also isomerize and retro-aldolize sugars, but at much lower reaction rates than Sn-Beta zeolite.[15–17]

It is widely accepted that isolated Sn centers embedded in siliceous zeolite frameworks catalyze the isomerization and retro-aldolization of carbohydrates.[17–20] Although recent experimental studies evidence a considerable heterogeneity of Sn speciation in different Sn-Beta zeolites,[21–23] there is an agreement that the active sites are partially hydrolyzed lattice Sn sites bearing an extraframework OH ligand (open Sn sites).[24–28] DFT calculations show that the cooperative action between the strong Lewis acid sites and neighboring proton-donating groups results in a favorable reaction path for the hydride shift reaction, which is the key step in sugar isomerization.[20,29–34] Although theory predicts that confinement should have only minor influence on the intrinsic reactivity of the cooperative reaction centers, zeolite topology will strongly affect the adsorption and diffusion of carbohydrates in the micropores.[32] The influence of the zeolite topology on carbohydrate isomerization has not been systematically studied yet by experiments.

Given the flexibility of Sn sites in Beta zeolite to catalyze reactions important to biobased chemistry such as triose and hexose isomerization and retro-aldolization of hexoses,[17,27,35–37] one would expect that similar chemistry is possible in other zeolites. In cases where mass transport limitations occur, secondary systems of larger pores could potentially increase the performance. For example, by introducing secondary pore systems and nanostructuring,[38] the catalytic performance of Sn-MFI zeolite could be substantially improved.[39–41]

Synthesis of Sn-modified zeolites is a challenging task. Direct hydrothermal synthesis of Sn-zeolites is cumbersome and so far limited to Sn-MFI[12,13] and Sn-Beta.[42,43] Direct hydrothermal synthesis suffers from very long reaction times, the use of fluoride-containing media, and relatively low Sn content of the final zeolite. To facilitate the hydrothermal synthesis, various approaches including for example the utilization of Sn–Si mixed oxide composites as the starting substrates[44] and the use of steam-assisted procedures[45] have been discussed. Besides such direct synthesis routes, several groups have reported in recent years alternative approaches to introduce Sn into the zeolite. Zeolites with high Sn content can be prepared by chemical vapor deposition of $SnCl_4$ on dealuminated zeolites. However, these zeolites contain both framework and extraframework Sn species.[46,47] Sn incorporation at framework positions can be improved by making use of mesoporous zeolites.[7,39,47] Hermans and co-workers developed a method for the preparation of Sn-Beta containing up to 10 wt% Sn, nearly exclusively at framework positions, by solid-state impregnation of dealuminated Beta zeolite with $Sn(OAc)_2$,[19,48] while Tang *et al.* used $Sn(CH_3)_3Cl_2$.[49]

A similar approach based on impregnation of dealuminated zeolite was developed by Sels and co-workers.[50,51] We have recently reported a methodology providing improved control over Sn speciation by reacting well-dehydrated dealuminated Beta zeolite with $SnCl_4$ in an inert atmosphere.[20] Careful washing of the modified zeolite with dry methanol allows avoiding extraframework Sn (EFSn) species.

In this work, we explore the utility of our post-synthetic Sn modification method developed for Beta zeolite[20] for the synthesis of Sn-modified zeolites with MWW, MOR and MFI topologies (Fig. 2). We also investigate how the hierarchical structuring and the presence of secondary mesoporous systems influence the Sn incorporation process. The synthesized materials are extensively characterized for their textural, morphological and Lewis acidic properties and their catalytic properties are assessed by studying their catalytic performance in three representative model carbohydrate conversion reactions, namely, (i) the conversion of 1,3-dihydroxyacetone (DHA) to methyl lactate, (ii) the isomerization of glucose to fructose and (iii) the retro-aldol condensation of glucose, fructose and sucrose to lactates. The physico-chemical properties and catalytic reactivity of the new materials are benchmarked against those of the Sn-Beta catalysts prepared by direct hydrothermal (fluoride) synthesis and by post-synthetic modification methods.

2. Experimental

2.1. Chemicals

Nitric acid (65% in water, Merck), NaOH (>98%, Sigma-Aldrich), $SnCl_4$ (99%, Sigma-Aldrich), tetraethylorthosilicate (TEOS, synthesis grade, Merck), HF (40% in H_2O, Merck), $SnCl_4{\cdot}5H_2O$ (98%, Acros), methanol (>99.8%, Biosolve), tetraethylammonium hydroxide (TEAOH, 35% in H_2O, Sigma) 1,3-dihydroxyacetone (dimeric form, >97%, Sigma Aldrich), D-glucose (99.5%, Sigma Aldrich), D-fructose (99%, Sigma Aldrich), sucrose (>99%, Sigma Aldrich), silica gel (Davisil

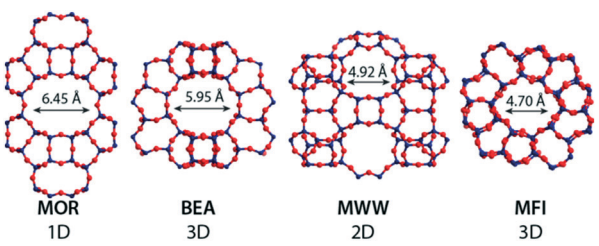

Fig. 2 Zeolite topologies used for Sn functionalization in the present study.

Grade 646, Sigma Aldrich), hexamethyleneimine (HMI, 99%, Sigma Aldrich), cetyl trimethylammonium bromide (CTAB, 96%, Sigma Aldrich), tetrapropylammonium hydroxide (TPAOH, 40 wt% in H_2O, Merck), *N*-phenylaminopropyl trimethoxysilane (95%, ABCR), tetrapropylammonium bromide (Alfa Aesar, 98%) were used as-received without further purification.

2.2. Materials

2.2.1. Hydrothermal synthesis of Sn-zeolites

[Sn]-Beta-HF. [Sn]-Beta-HF was synthesized according to a procedure by Corma and co-workers.[42] To a mixture of tetraethylorthosilicate (TEOS, 14.03 g, 67 mmol) and tetraethylammonium hydroxide (15.42 g of a 35 wt% aqueous solution, 37 mmol N), $SnCl_4{\cdot}5H_2O$ (0.24 g, 0.68 mmol) was added and the mixture was stirred overnight. Afterwards, a part of the volatiles was evaporated and HF (40% aqueous solution, 1.5 mL) was added. The resulting solid gel was thoroughly mixed. The final composition of the gel was 1 SiO_2 : 0.54 TEAOH : 0.52 HF : 0.01 Sn : 7.5 water. Dealuminated nano-sized Beta (final Si/Al = 14), prepared by refluxing nano-sized Beta in 65% aq. HNO_3 (ref. 20), was added to the gel (1 wt% based on silica) and the mixture was transferred into a Teflon-lined steel autoclave. The mixture was kept at 140 °C for 40 days in static mode. The resulting materials were thoroughly washed with water and ethanol and dried in air. The template was removed by calcination at 550 °C for 10 h after heating to this temperature at a rate of 1 °C min^{-1}.

[Sn]-MFI-F. [Sn]-MFI-F was synthesized according to a modified procedure by Dapsens *et al.*[12] A solution of 0.50 g $SnCl_4{\cdot}5H_2O$ (1.4 mmol) in 10 mL demineralized water was slowly added to a solution of NH_4F (5.35 g, 14.5 mmol) in 25 mL demineralized water and the mixture was stirred for 30 min. The resulting solution was then added slowly to a solution of TPABr (8.3 g, 31 mmol) and TPAOH (2.9 g, 40 wt% aq. solution, 5.7 mmol N) in 54 mL demineralized water. After stirring for 30 minutes, fumed silica (8.6 g, 143 mmol) was added and the mixture was stirred for 3 h. The gel was then transferred to a Teflon-lined steel autoclave and statically heated at 200 °C for 11 days. The final material was obtained by calcination at 550 °C for 6 h (1.5 °C min^{-1}).

2.2.2. Zeolite precursors for post-synthetic Sn incorporation

Mesoporous MFI (MFI-meso). Mesoporous MFI (MFI-meso) zeolite was prepared by desilication of MFI-bulk (Si/Al = 40), according to a method reported by Tempelman *et al.*[52] MFI-bulk (1.66 g) was suspended in a 50 mL 0.2 M NaOH solution and stirred at 65 °C for 30 minutes. Subsequently, the product was filtered and washed thoroughly with demineralized water. The resulting material was denoted MFI-meso.

MFI nanocrystals (MFI-nano). MFI nanocrystals (MFI-nano) were prepared following a procedure reported by Serrano *et al.*[53] A mixture (A) was prepared by adding TEOS (12.4 g, 59.6 mmol) to a 40% tetrapropyl ammonium hydroxide solution (3.9 mL, 7.7 mmol). A second solution (B) was prepared by dissolving $NaAlO_2$ (0.245 g, 2.99 mmol) in 23.49 g water. After dissolving, solution B was added to mixture A. The resulting mixture was refluxed for 20 h at 90 °C under stirring. To this mixture, *N*-phenylaminopropyl trimethoxysilane (2.07 g, 7.9 mmol) was added and the mixture was kept refluxing for another 6 h at 90 °C. After this period, the resulting gel was transferred to a Teflon-lined autoclave and heated at 170 °C for 5 days. The solid was recovered by filtration followed by washing with copious amounts of water. The organic templates were removed by calcination at 550 °C (1 °C min^{-1}) in flowing artificial air for 6 h. The obtained material is referred to as MFI-nano.

MFI nanosheets (MFI-NS). MFI nanosheets (MFI-NS) were synthesized according to a modified procedure by Zhu *et al.*[54] To a mixture of TEOS (15.6 g, 73 mmol) and $Al(NO_3)_3{\cdot}9H_2O$ (0.547 g, 1.46 mmol) in water (24 g), a solution of NaOH (0.61 g, 15.3 mmol) and previously prepared $C_{22}H_{45}N(CH_3)_2(CH_2)_6N(CH_3)_2C_3H_7Br_2$ ($C_{22\text{-}6\text{-}3}$ template, 3.15 g)[54] in water (30 g) was added. The mixture was shaken thoroughly for 5 min and then stirred for 1 h. The mixture was then transferred to a Teflon-lined steel autoclave and rotated (20 rpm) for 10 days at 150 °C. The resulting material was filtered, washed thoroughly with demineralized water and ethanol and dried in air. Calcination at 550 °C (10 h, 1 °C min^{-1}) was carried out to remove the template from the material.

MWW-precursor and MWW-bulk. MWW-precursor and MWW-bulk zeolites were prepared according to a modified procedure by Tempelman *et al.*[55] In a typical synthesis, silica gel (5.85 g) was mixed with hexamethyleneimine (2.97 g) in a round-bottom flask. To the resulting suspension, a solution of sodium hydroxide (0.385 g) and sodium aluminate (0.48 g) in water (30 mL) was added and the resulting mixture was stirred overnight at room temperature. Afterwards, the gel was transferred to a Teflon-lined stainless steel autoclave and kept at 150 °C for 7 days under rotation (60 rpm). The as-synthesized material was denoted MWW-precursor. MWW-bulk was obtained by calcination of the MWW-precursor at 450 °C for 6 h (1 °C min^{-1}).

Nanostructured MWW zeolite (MWW-nano). Nanostructured MWW zeolite (MWW-nano) was prepared following a modified procedure by Tempelman *et al.*[55] Silica gel (5.85 g) was mixed with hexamethyleneimine (HMI, 2.97 g) in a round-bottom flask. To the suspension, a solution of sodium hydroxide (0.385 g) and sodium aluminate (0.48 g) in water (30 mL) was added and the resulting mixture was stirred overnight at room temperature. After stirring overnight, dimethyloctadecyl(trimethylsilylpropyl)ammonium chloride (23.0 g of 60 wt% solution in methanol) was added and stirring was continued for 4 h. The gels were transferred to a Teflon-lined stainless steel autoclave and kept at 150 °C for 7 days under rotation (60 rpm). The final material was obtained by calcination at 450 °C for 6 h (1 °C min^{-1}). These materials were denoted MWW-nano.

Delaminated MWW zeolite (MWW-delam). Delaminated MWW zeolite (MWW-delam) was prepared according to a method described by Corma and co-workers.[56] MWW-

precursor was used as the starting material for the delamination procedure. To 1 g of MWW-precursor (3.9 mL), an aqueous solution (29 wt%) of cetyltrimethylammonium bromide (CTAB) was added. After a homogeneous mixture was obtained, 1.2 g TPAOH (40 wt% in water) was added. The final mixture was heated for 16 h at 80 °C. After this, the mixture was ultra-sonicated for 1 h. Finally, the pH was adjusted to 2 and the mixture was stirred for 1 h and subsequently filtered. To remove the organic constituents, the solid was calcined in a He/O_2 (4 : 1) flow at 550 °C for 6 h.

Nanostructured MOR (MOR-nano) zeolite. Nanostructured MOR (MOR-nano) zeolite was prepared by ball-milling of commercial mordenite (Si/Al = 11, Akzo Nobel, now Albemarle). Typically, 6 g of zeolite was placed in a tungsten carbide (WC) ball-milling vessel. To the zeolite, 6 g of H_2O was added together with 4 WC balls with a diameter of 10 mm. The ball-milling vessel was then placed in a Retsch PM 400 planetary ball-milling machine. The zeolites were ball-milled for 8 h at a rotation speed of 240 rpm and the rotation was altered to the opposite direction every 15 min. After the ball-milling procedure, the solid was recovered by adding 20 mL of water. The suspension was ultra-sonicated for 99 min and subsequently centrifuged for 5 min at a rotation speed of 5000 rpm. The collected materials were dried in air and denoted MOR-nano.

2.2.3. Sn modification. The calcined zeolites were modified with Sn according to a procedure by van der Graaff *et al.*[20] Dealumination was performed by refluxing the zeolites in 65 wt% aqueous nitric acid (50 mL g^{-1}) at 110 °C for 16 h. Subsequently, the zeolites were filtered and washed extensively with demineralized water until the pH of the filtrate was neutral. Sn grafting was carried out by first drying 2 g of dealuminated zeolite *in vacuo* at 170 °C in a Schlenk flask for 3 h. After cooling to 100 °C, anhydrous $SnCl_4$ (3 mL) was added and the mixture was allowed to stand for 16 h under an Ar atmosphere at 100 °C. The zeolite was then cooled to room temperature and methanol was added to quench the reaction. After thorough washing with methanol, the zeolites were collected by centrifugation and dried in air. The final materials were obtained after calcination in static mode at 550 °C for 5 h (1 °C min^{-1}). The resulting materials are denoted by the prefix 'Sn-'.

2.3. Characterization

Elemental analysis. Elemental analysis was performed by ICP-OES on a Spectro Ciros CCD ICP optical emission spectrometer with axial plasma viewing. For analysis of the materials, an equivolumetric mixture of HF (40 wt% in water), HNO_3 (65 wt% in water) and water was used to dissolve the zeolites. X-ray diffraction analysis was carried out using a Bruker D2 Cu Kα diffractometer. The diffractograms were recorded in the range of $5° > 2\theta > 60°$ with an interval of 0.012° (0.4 s per step).

Fourier-transform infrared (FTIR). Fourier-Transform Infrared (FTIR) spectra of adsorbed pyridine and acetonitrile-D3 were recorded using a Bruker Vertex V70v system. A total of 32 spectra at a resolution of 2 cm^{-1} were averaged. The samples were prepared as thin self-supporting wafers of 5–15 mg cm^{-2} density and placed inside a controlled-environment infrared transmission cell.

For pyridine adsorption, the catalyst wafer was heated to 550 °C at a rate of 2 °C min^{-1} under vacuum ($p < 5 \times 10^{-6}$ mbar) and maintained at this temperature for 3 h. After cooling to 100 °C, pyridine was introduced into the cell under static vacuum for 30 min. Physisorbed pyridine was removed *in vacuo* for 30 min. The evacuated sample containing chemisorbed pyridine was heated to 200 °C (5 °C h^{-1}) and after 30 minutes spectra were recorded. Background correction was performed by subtracting the spectrum of the dehydrated wafer recorded at 200 °C. Integration of the signals for determining the amount of Lewis and Brønsted acid sites was performed using the Fityk curve fitting program.

Prior to the adsorption of CD_3CN, the catalyst wafer was heated to 550 °C (2 °C min^{-1}) and kept at this temperature for 1 h under dynamic vacuum ($p < 5 \times 10^{-6}$ mbar). After cooling down to 30 °C, the vacuum pump was disconnected and CD_3CN was added stepwise to the evacuated cell until the intensity of the absorption bands at ν = 2308–2316 cm^{-1} did not increase anymore. Then, the CD_3CN line was disconnected and dynamic vacuum was reconnected. Spectra were recorded after evacuation at 30 °C for 1, 2, 3, 4, 5, 10, 30 and 60 minutes, with a resolution of 2 cm^{-1} and as an average of 8 scans. Background correction was performed by subtracting the spectra of the dehydrated samples recorded at 30 °C.

X-ray photoelectron spectroscopy (XPS). X-ray photoelectron spectroscopy (XPS) measurements were performed on a Thermo Scientific K-Alpha XPS apparatus equipped with a monochromatic small-spot Al Kα X-ray source and a 180° double focusing hemispherical analyzer with a 128-channel detector. The background pressure was 2×10^{-9} mbar. Samples were prepared by pressing the solids onto a carbon film. Analysis of the XPS data was performed using the CasaXPS program.

Ar sorption experiments. Ar sorption experiments were performed on a Micromeritics ASAP 2020 at −186 °C. Prior to measurement, the samples were outgassed for 10 h at 350 °C. For all sorption measurements, the typical sample weight was 100 mg. Textural properties were determined using the BET and BJH methods applied to the adsorption branch of the isotherms. Micropore volume was determined using the *t*-plot method. For MFI nanosheet materials, the NL-DFT method was used (Ar on oxides, cylindrical pores, no regularization).

UV-Vis spectra. UV-Vis spectra were recorded on a Shimadzu UV-2401 PC spectrometer in a diffuse-reflectance mode with a 60 mm integrating sphere. $BaSO_4$ was used as the reference. The reflectance values were transformed into Kubelka–Munk units.

Transmission electron microscopy (TEM). Transmission Electron Microscopy (TEM) micrographs were acquired on a FEI Tecnai 20 transmission electron microscope (FEI

Company) at an accelerating voltage of 200 kV with a LaB_6 filament. TEM sample preparation involved sonication of the samples in pure ethanol and deposition of a few droplets of the resulting suspension on a 200 mesh Cu TEM grid with a holey carbon support film. TEM images were recorded at different magnifications using a Gatan 1k × 1k CCD camera. Scanning electron microscopy (SEM) was performed using a Philips environmental FEIXL-30 ESEM FEG in high-vacuum mode at low voltage.

2.4. Catalytic activity measurements

1,3-Dihydroxyacetone isomerization. In a typical experiment, 1,3-dihydroxyacetone was dissolved in methanol (0.25 M). An amount of 2.5 mL of this solution and 40 mg of catalyst were added into a 4 mL thick-walled glass vial. Reactions were performed at 70 °C or 90 °C under stirring (500 rpm) by heating the vial in a thermostated oil bath. After reaction, the mixtures were quenched and directly analyzed by GC-FID with *n*-decane as the external standard on a Shimadzu GC-17 A gas chromatograph equipped with a Restek Rxi-5 ms column (30 m × 0.25 mm, d_f = 0.25 μm). 2-Hydroxy-3-methoxypropanal (HMP, by-product in the conversion of DHA to methyl lactate) yields were estimated using the relative response factor of methyl lactate.

Glucose isomerization. In a typical experiment, 40 mg catalyst and 2.5 mL of a 125 mM glucose in water solution were introduced into a 4 mL thick-walled reaction vial. The reactions were carried out at 100 °C. Reaction mixtures were analyzed by HPLC using a Prevail carbohydrate column (Grace, 4.6 × 250 mm column, 5 μm particle size) coupled to a Shimadzu ELSD-II detector. HPLC analysis was performed at room temperature with acetonitrile/water (65/35 v/v) as the eluent at a flow rate of 0.75 mL min^{-1}. ELSD analysis was carried out at 50 °C and a N_2 pressure of 3.50 bar.

2.4.3. Retro-aldol condensation of hexose sugars. In a typical experiment, 112 mg of sugar (glucose, fructose or sucrose), 80 mg of catalyst and 5 mL of methanol were introduced into a 10 mL steel autoclave. After sealing, the autoclave was heated to 160 °C for 20 h in a temperature-controlled aluminum heating block on a stirring plate (500 rpm). Reaction mixtures were analyzed by GC-FID with *n*-decane as the external standard on a Shimadzu GC-17 A gas chromatograph equipped with a Restek Rxi-5 ms column (30 m × 0.25 mm, d_f = 0.25 μm).

3. Results

3.1. Synthesis and characterization

We employed a two-step post-synthetic modification strategy[20] to prepare Sn-zeolites with different framework topologies and textures. First, the parent Al-zeolite is dealuminated by an acid treatment to generate internal silanol nests, which are then used as the grafting sites for anhydrous $SnCl_4$ in the second step. XRD characterization (Fig. 3) of the synthesized materials evidences the preservation of the zeolite structure and crystallinity during the preparation. A similar conclusion can be drawn from the analysis of the textural properties of the parent and modified zeolites (Table 1). The physisorption data confirm that the dealumination–$SnCl_4$ treatment, in general, did not strongly affect the zeolite texture. Even for MFI-NS, the micropore volume and specific surface area did not change significantly after Sn incorporation.

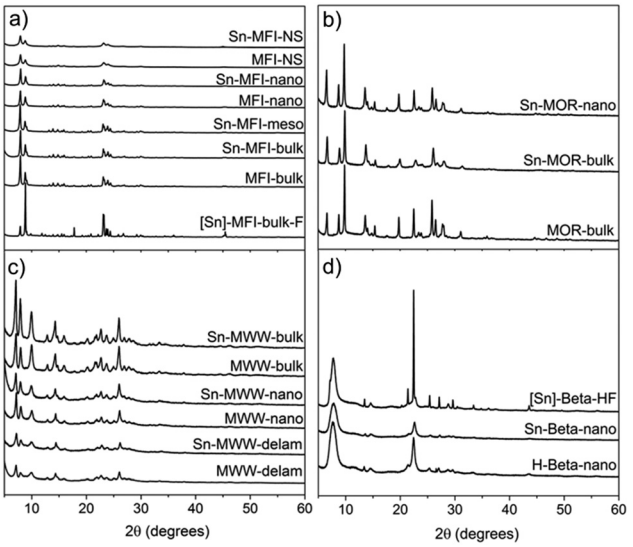

Fig. 3 XRD patterns of the parent and functionalized a) MFI, b) MOR, c) MWW and d) Beta materials.

All mesoporous materials were also characterized by a high level of crystallinity. Desilication used to introduce mesopores into MFI-bulk did not result in the formation of an amorphous by-product as could be seen from the very similar diffraction patterns of MFI-bulk and Sn-MFI-meso

Table 1 Textural properties of the zeolites

Zeolite	V_{micro} ($cm^3\ g^{-1}$)	V_{meso} ($cm^3\ g^{-1}$)	S_{micro} ($m^2\ g^{-1}$)	S_{meso} ($m^2\ g^{-1}$)	S_{BET} ($m^2\ g^{-1}$)
MWW-bulk	0.15	0.08	260	71	391
Sn-MWW-bulk	0.14	0.16	265	78	397
MWW-nano	0.08	0.09	193	44	276
Sn-MWW-nano	0.08	0.40	101	162	289
MWW-delam	0.11	0.16	223	81	449
Sn-MWW-delam	0.09	0.19	187	98	392
MFI-bulk	0.13	0.13	257	85	392
Sn-MFI-bulk	0.13	0.08	269	85	367
Sn-MFI-meso	0.12	0.27	244	137	391
MFI-nano	0.13	0.08	279	54	361
Sn-MFI-nano	0.12	0.13	251	73	398
MFI-NS	0.11[a]	0.44	122	338[b]	460
Sn-MFI-NS	0.10[a]	0.44	112	329[b]	441
[Sn]-MFI-bulk-F	0.14	0.02	274	13	305
MOR-bulk	0.15	0.07	292	49	369
Sn-MOR-bulk	0.14	0.07	288	42	354
Sn-MOR-nano	0.11	0.17	218	62	305
Beta-nano	0.15	0.29	302	141	479
Sn-Beta-nano	0.15	0.36	307	171	518
[Sn]-Beta-HF	0.22	0.06	444	52	584

[a] Determined by NL-DFT (Ar on oxides, cylindrical pores, no regularization). [b] External surface area.

(Fig. 3a). Ball-milling of MOR-bulk, used to obtain smaller crystals (MOR-nano), and subsequent Sn modification also did not appreciably affect the crystallinity (Fig. 3b). Similarly, high crystallinity of the nanostructured Sn-MFI-NS, Sn-MFI-nano, Sn-MWW-nano and Sn-MWW-delam materials is confirmed by the XRD data.

The nanostructured materials had significantly higher mesopore volumes compared to their bulk counterparts. For example, the nanostructuring of MWW zeolite to form Sn-MWW-nano resulted in a mesopore volume of 0.40 $cm^3\ g^{-1}$ compared to the value of 0.16 $cm^3\ g^{-1}$ for Sn-MWW-bulk. Sn-MFI-meso, prepared by sequential desilication, dealumination and $SnCl_4$ treatment of MFI-bulk, contained a significant amount of mesopores (0.27 $cm^3\ g^{-1}$) compared to its bulk analogue (0.08 $cm^3\ g^{-1}$, likely voids between zeolite particles). The reduction of crystallite size of MOR-bulk by ball-milling led to a lower micropore volume in Sn-MOR-nano and a higher mesopore volume from 0.07 $cm^3\ g^{-1}$ to 0.17 $cm^3\ g^{-1}$, the latter likely due to the presence of intercrystalline voids.

Fig. 4 presents SEM and TEM micrographs of the calcined zeolites. These data reveal that the morphology of the zeolites is generally not affected by Sn functionalization. This is in line with our previous findings[20] and the textural and structural data derived from Ar experiments and XRD. Only for Sn-MFI-meso, cracks have appeared in the zeolite crystals suggesting that the desilication procedure affects the mechanical stability.

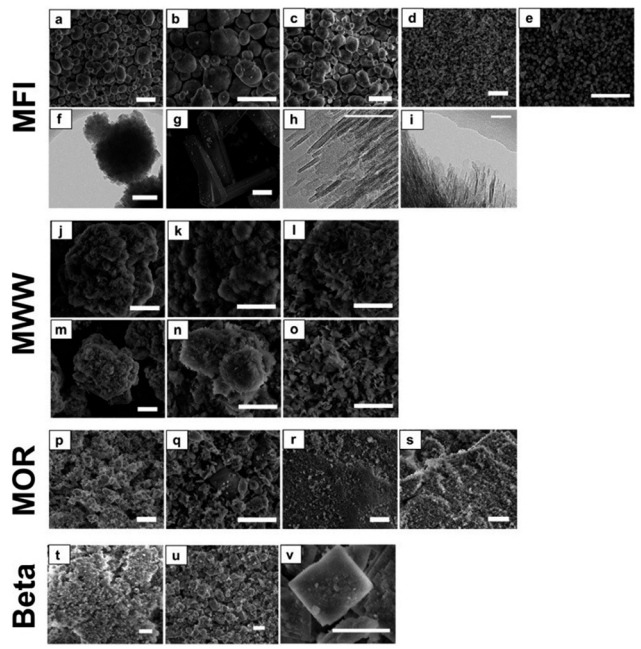

Fig. 4 Electron microscopy results (scale bars are 5 μm, unless otherwise indicated) for a) MFI-bulk, b) Sn-MFI-bulk, c) Sn-MFI-meso, d) MFI-nano, e) Sn-MFI-nano, f) Sn-MFI-nano (scale: 200 nm), g) [Sn]-MFI-bulk-F (scale: 10 μm), h) MFI-NS (scale: 50 nm), i) Sn-MFI-NS (scale: 50 nm), j) MWW-bulk, k) MWW-nano, l) MWW-delam, m) Sn-MWW-bulk, n) Sn-MWW-nano, o) Sn-MWW-delam, p) MOR-bulk, q) Sn-MOR-bulk, r) MOR-nano, s) Sn-MOR-nano, t) Beta-nano, u) Sn-Beta-nano and v) [Sn]-Beta-HF (scale: 2 μm).

The very large particles of [Sn]-MFI-F (*ca.* 60 μm) have the typical coffin-shaped morphology of intergrown ZSM-5. [Sn]-Beta-HF consists of plate-shaped particles of around 2 μm, which are typically observed when relatively high amounts of Sn (Si/Sn = *ca.* 100) are incorporated in Beta.[57] Sn-MFI-nano consists of agglomerates with a size of about 250 nm, which themselves are agglomerates of small nanosized (*ca.* 10 nm) crystallites (Fig. 4e and f). The MFI nanosheets (MFI-NS) display a typical sheet-like structure with a thickness of about 2–3 nm. A similar structure is observed for the MWW materials and particularly for the delaminated MWW (MWW-delam). For the MOR zeolites, the particle size of the parent MOR-bulk is reduced from about 2 μm to ~300 nm by ball-milling.

The chemical composition of the zeolites at the different stages of the two-step Sn modification procedure was determined by ICP analysis (Table 2). The efficiency of Al extraction by acid treatment is to a large extent determined by the zeolite topology and its pore size. Nearly all Al can be removed from the large-pore MOR and Beta zeolites (MOR = 6.45 Å, 92–93%; Beta = 5.95 Å, >99%). However, the efficiency of Al extraction from the medium-pore MWW and MFI zeolites was much lower (57% and 32%, respectively). This should be attributed to the higher stability of framework Al in these materials.[58] The generation of mesoporosity improves the efficiency of Al extraction. 73% and 62% of lattice Al can be removed from the nano-structured MWW-delam and MFI-NS zeolites. We ascribe this to a combination of the improved transport characteristics and at the same time the decreased stability of lattice Al sites due to the higher density of defects in these nanostructured materials.

The efficiency of Sn incorporation (I_{eff}, Table 2), defined as the ratio of the incorporated Sn to the amount of removed Al, correlates well with the efficiency of the first Al extraction step. Here, we assume that our two-step procedure introduces a single lattice Sn site for each framework Al removed. We should note here that the current efficiency parameter does not account for the potential presence of extraframework aluminium in the starting materials.

Table 2 Elemental composition of the synthesized materials

Catalyst	Si/Al (ICP) Parent	Si/Al (ICP) Final	Si/Sn (ICP)	Si/Sn (XPS)	Si/Al (XPS)	I_{eff}[c] (%)
Sn-MWW-bulk	15	35	65	36	89	40
Sn-MWW-nano	18	33	73	37	47	54
Sn-MWW-delam	15	56	32	23	110	64
Sn-MFI-bulk	40	53	270	135	66	60
Sn-MFI-meso	30	61	97	71	75	61
Sn-MFI-nano	26	55	88	76	90	56
Sn-MFI-NS	52	138	67	67	214	125[a]
[Sn]-MFI-bulk-F	n.d.[b]	n.d.[b]	109	38	n.d.[b]	—
Sn-MOR-bulk	11	138	33	35	n.d.[b]	33
Sn-MOR-nano	11	160	57	35	670	19
Sn-Beta-nano	12	635	80	53	n.d.[b]	14
[Sn]-Beta-HF	n.d.[b]	n.d.[b]	95	66	n.d.[b]	—

[a] Contains significant amounts of EFSn. [b] n.d. = not detected. [c] Incorporation efficiency (amount of Sn incorporated per removed Al).

Higher Sn loading could be achieved for the nanostructured MWW and MFI compared to the corresponding bulk zeolites. Whereas Sn-MMW-bulk had a Si/Sn ratio of 65, it amounted to 32 for Sn-MWW-delam. Only trace amounts of Sn could be detected in Sn-MFI-bulk (Si/Sn = 270), while the Si/Sn ratios for Sn-MFI-nano, Sn-MFI-meso and Sn-MFI-NS were equal to 88, 97 and 67, respectively. The highest loading of Sn was achieved for the MFI nanosheets giving formally a 125% Sn incorporation efficiency. This implies that a major fraction of Sn was introduced as EFSn species rather than lattice Sn sites.

I_{eff} values were the highest for Sn-MWW (40%) and Sn-MFI (60%). The lower efficiencies obtained for the large-pore Beta (14%) and MOR (19–33%) zeolites are most likely due to the higher Al content in the commercial Beta and MOR starting materials containing a much larger amount of defects that are more difficult to heal by Sn^{4+}.[20] We argue that only those species that are strongly bound to the zeolite framework remain during the methanol washing step, which removes weakly bound Sn-chloride species.

Substantial Al and Sn gradients over the zeolite crystals are evident from comparison of the bulk Si/Sn ratios measured by ICP elemental analysis and the surface Si/Sn ratios determined by XPS (Table 2). In general, the Sn content at the external surface of the crystals was higher than the bulk content, while the surface Al concentration was lower than that in the bulk. These differences were most pronounced for Sn-MWW-bulk and Sn-MFI-bulk consistent with a proposal on the mass transport limitations of mobile Al and Sn species during delamination and stannation. Accordingly, the difference between the bulk and surface Al and Sn contents was the smallest for the nanostructured zeolites.

FTIR spectroscopy of adsorbed pyridine was employed to quantitatively assess the acid properties of selected zeolites (Fig. 5). Sn-MOR-bulk, Sn-MWW-nano, Sn-MWW-delam, Sn-MFI-bulk, Sn-MFI-meso and Sn-MFI-nano all showed both characteristic signals for Brønsted (ν = 1545 cm^{-1}) and Lewis (ν = 1450 cm^{-1}) acid sites. Quantification of these contributions (Table 3) shows that the amount of BAS and LAS trend with the Al and Sn content, respectively. Therefore, Al remaining in the zeolite upon dealumination is present at the original lattice positions giving rise to Brønsted acid sites (BAS). Lewis acid sites (LAS) are due to lattice Sn sites. Only for Sn-MWW-nano, the amount of BAS (425 μmol g^{-1}) was significantly lower than the Al content (501 μmol g^{-1}). Concomitantly, the intensity of the signal due to LAS was significantly higher compared to the Sn content, indicating that both extraframework aluminum and lattice Sn contribute to the overall Lewis acidity.

A qualitative insight into the nature of intrazeolite Sn was obtained by UV-Vis spectroscopy and FTIR spectroscopy of adsorbed CD_3CN (Fig. S3 and S4, respectively, in the ESI†). Previous studies assigned the UV-vis absorption band at 200 nm to lattice Sn sites and bands in the 240 nm region to EFSn.[19,46] The former feature dominates all spectra of the Sn-modified materials suggesting the predominance of the isolated Sn speciation. Although previous studies reported a beneficial effect of hierarchical structuring on the uniformity of the Sn species in Sn-Beta prepared by post-synthetic Sn modification,[39] the results in Fig. S3† do not evidence the generality of this effect for other zeolite topologies. FTIR spectroscopy of the CD_3CN adsorption probe is commonly employed to differentiate between the more Lewis acidic open and the less reactive closed lattice Sn species. The relative population of the closed and open lattice Sn sites is assessed from the relative intensities of the respective characteristic bands at 2308 and 2316 cm^{-1} in the FTIR spectra of adsorbed acetonitrile.[26] Our data indicate that the closed Sn sites are more abundant in the MFI- and MWW-type zeolites than those in the Sn-Beta materials. Given the much higher Sn loading in Sn-MWW than that in Sn-Beta (Table 2), the spectroscopic results (Fig. S4†) suggest a comparable concentration of the strongly Lewis acidic open Sn sites in both material types. A single type of Sn site was identified for Sn-MOR with a somewhat lower Lewis acidity than the open sites in Sn-Beta and Sn-MWW as is probed by CD_3CN adsorption.

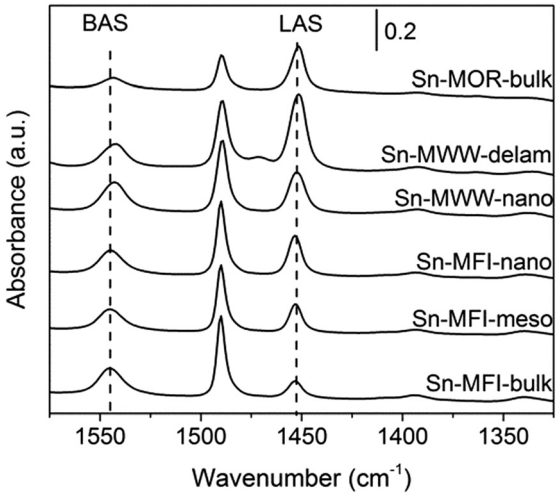

Fig. 5 FTIR spectra of adsorbed pyridine on selected Sn-containing zeolite catalysts. Absorption bands due to pyridine interacting with Brønsted and Lewis acid sites are indicated as BAS and LAS, respectively.

Table 3 Quantification of the Brønsted and Lewis acid sites of representative catalysts by FTIR spectroscopy of pyridine adsorption at 200 °C according to Datka *et al.*[59]

Catalyst	Al content[a] (μmol g^{-1})	BAS[b] (μmol g^{-1})	Sn content[a] (μmol g^{-1})	LAS[c] (μmol g^{-1})
Sn-MFI-bulk	319	353	57	85
Sn-MFI-meso	275	281	158	165
Sn-MFI-nano	317	299	172	171
Sn-MWW-nano	501	425	197	279
Sn-MWW-delam	320	313	464	472
Sn-MOR-bulk	112	114	471	281

[a] Determined by ICP. [b] Based on the intensity of the band at 1545 cm^{-1}. [c] Based on the intensity of the band at 1450 cm^{-1}.

The post-synthetic introduction of Sn yields a higher concentration of the open sites in the final materials. More detailed information on the influence of zeolite topology on lattice Sn speciation cannot be accessed with this rather low-sensitive technique. It requires a more detailed study employing advanced characterization methods (*e.g.* DNP NMR),[23] which is beyond the scope of the current work.

3.2. Catalytic activity

The influence of the zeolite topology, the Sn content and the textural properties on the catalytic performance of the Sn-modified zeolites was evaluated in three different carbohydrate conversion reactions. Table 4 lists the results for the catalytic isomerization of DHA in methanol after a reaction time of 2 h. The Sn-Beta zeolites were the only ones exhibiting high selectivity to methyl lactate. The other zeolites produced side-products such as 2-hydroxy-3-methoxypropanal (HMP). Scheme 1 depicts reaction pathways from DHA to ML and HMP. HMP is formed by the isomerization of DHA to glyceraldehyde followed by condensation with methanol.

Only a very low activity was observed for Sn-MOR-bulk and Sn-MOR-nano at 70 °C and 90 °C. Bulk Sn-MFI and Sn-MWW zeolites were moderately active. For Sn-MWW, ML yields in ranges of 25–32% and 69–71% were obtained at 70 °C and 90 °C, respectively. The ML yields for the hierarchical Sn-MFI zeolites were higher (19–33%) than those for the Sn-MFI-bulk (12%) and [Sn]-MFI-bulk-F (12%) samples. In all cases, pyruvaldehyde amounted to less than 5% of the products.

The time courses of the DHA conversion for the Sn-Beta, Sn-MFI and Sn-MWW zeolites are shown in Fig. 6. Among the bulk zeolites, Sn-Beta showed the highest catalytic performance. Quantitative conversion of DHA to ML is reached after 1 h with Sn-Beta-bulk, whereas the other two bulk zeolites only achieve yields of 19% and 44% after 4 h. The initial ML reaction rate was much higher for [Sn]-Beta-HF (160 h^{-1}) than those for Sn-MFI-bulk (21 h^{-1}) and Sn-MWW-bulk (13 h^{-1}).

Table 4 Conversion of DHA to ML

			Yield (%)				
			70 °C		90 °C		TOF[a]
Catalyst	Si/Sn	Si/Al	ML	HMP	ML	HMP	(h^{-1})
Sn-MWW-bulk	65	35	25	32	69	2	13
Sn-MWW-nano	73	33	31	25	71	<1	17
Sn-MWW-delam	32	56	32	20	71	<1	8
Sn-MFI-bulk	270	53	12	11	34	17	21
Sn-MFI-meso	97	61	29	10	68	<1	17
Sn-MFI-nano	88	55	33	26	72	8	18
Sn-MFI-NS	67	138	19	6	56	11	7
[Sn]-MFI-bulk-F	109	n.d.	12	2	29	6	6
Sn-MOR-bulk	33	138	<1	46	14	47	—
Sn-MOR-nano	57	160	2	51	14	45	—
Sn-Beta-nano	80	635	92	<1	98	<1	61
[Sn]-Beta-HF	95	n.d.	>99	<1	>99	<1	160

Conditions: 40 mg cat, 2 h, 2.5 mL of 250 mM DHA in methanol. [a] At 70 °C, per Sn-site.

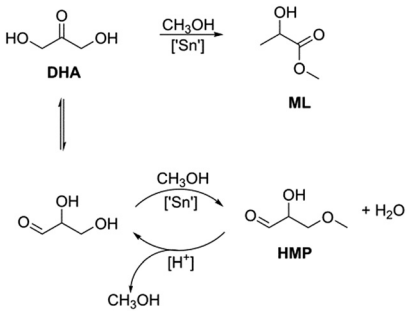

Scheme 1 Reaction pathways from DHA to ML and HMP over Sn-modified zeolites.

The benefit of hierarchical zeolite structuring on DHA conversion can be appreciated from Fig. 6b and c.

Mesoporous Sn-MFI zeolites allow reaching higher ML yields compared to their microporous counterpart, although with similar initial rates (Fig. 6b). For the MWW zeolites (Fig. 6c), the initial activities were also similar despite the considerable variation in Sn content (Table 4). As a result, the Sn-normalized initial rates became lower with increasing Sn content from 17 h^{-1} for Sn-MWW-nano to only 8 h^{-1} for Sn-MWW-delam. This might indicate that not all Sn sites are involved in the catalytic reaction. Significant amounts of HMP were formed in the early stages of the reaction, especially with Sn-MWW as catalysts (Fig. S1†). The HMP yield gradually decreased over time.

Next, we studied the activity of the materials in glucose-to-fructose isomerization at 100 °C in water (Scheme 2). The results of the catalytic tests are summarized in Table 5 and Fig. 7.

Among the investigated samples, only the large-pore Sn-MOR and Sn-Beta catalysts were active in glucose isomerization. The carbon balance for the Sn-Beta zeolites was poor (65–68%). Reaction in water for 2 h at 100 °C resulted in glucose and fructose yields of about 30% and a mannose yield of 5%. Much less fructose was formed with Sn-MOR (10%) after 6 h under otherwise identical conditions. All Sn-MWW and Sn-MFI zeolites showed negligible activity, except for Sn-MFI-nano that afforded a fructose yield of 3%. Although this result contrasts with previous reports on the beneficial effect of nanostructuring, it should be related to the different preparation method employed in this study, which is specifically designed to avoid EFSn species and leads to less exposed Sn-sites.

The reaction is much more sluggish over Sn-MOR-bulk and the carbon balance is similar for all reaction times (Fig. 7). Up to about 6 h, the reaction is highly selective to fructose. After 24 h, the reaction with the Sn-MOR-bulk zeolite stops at a glucose conversion of 25%. The fructose and mannose yields are 22% and 1%, respectively. The thermodynamic equilibrium for the glucose/fructose isomerization reaction is 43 : 57 at 100 °C.[9,60] Accordingly, we conclude that the Sn-MOR-bulk zeolite was deactivated, likely by humin-type side-products blocking the zeolite micropores. The one-

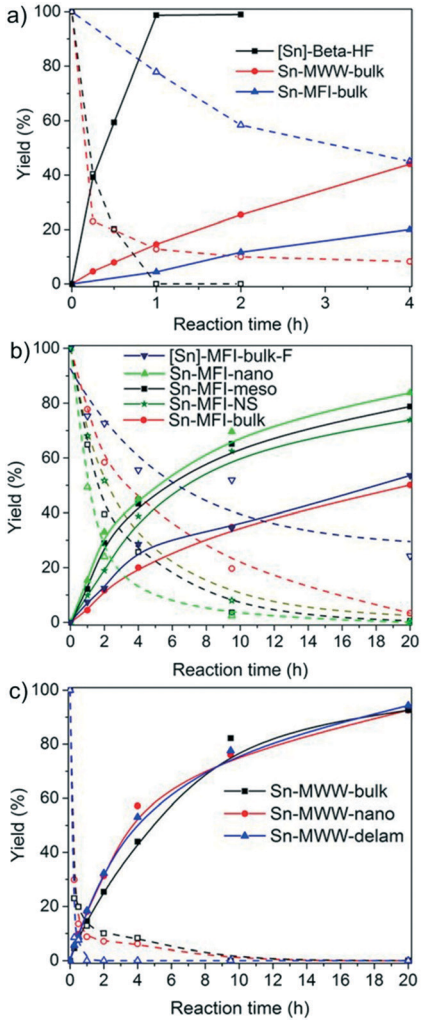

Fig. 6 Time-profiles for the DHA-to-ML conversion in the presence of a) [Sn]-Beta-HF, Sn-MFI-bulk and Sn-MWW-bulk, b) selected nanostructured MFI materials compared to Sn-MFI-bulk and c) nanostructured MWW materials compared to Sn-MWW-bulk. The solid lines represent ML, the dashed lines indicate DHA. Conditions: 40 mg cat, 2.5 mL of a 250 mM methanolic DHA solution, 70 °C.

dimensional pores of MOR are more susceptible to blockage than the three-dimensional pore system of Beta.

We further investigated the activity of the zeolites in the retro-aldolization of glucose, fructose and sucrose (Scheme 3). This reaction requires a higher temperature than the reactions investigated above. The results of the catalytic activity measurements are given in Table 6. The medium-pore zeolites Sn-MFI and Sn-MWW, which were inactive for glucose isomerization at 100 °C, performed well in the conversion of glucose to methyl lactate at 160 °C. ML yields up

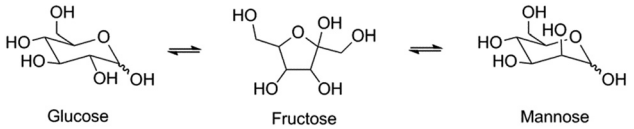

Scheme 2 Isomerization of glucose to fructose and mannose.

Table 5 Isomerization of glucose over Sn-modified zeolites

Catalyst	Si/Sn	$Y_{Glucose}$ (%)	$Y_{Fructose}$ (%)	$Y_{Mannose}$ (%)
Sn-MWW-bulk	65	>99	<1	<1
Sn-MWW-nano	73	>99	<1	<1
Sn-MWW-delam	32	>99	<1	<1
Sn-MFI-bulk	270	>99	<1	<1
Sn-MFI-meso	97	99	1	<1
Sn-MFI-nano	88	90	3	<1
Sn-MFI-NS	67	99	1	<1
[Sn]-MFI-bulk-F	109	>99	<1	<1
Sn-MOR	33	90	10	<1
Sn-MOR-nano	57	95	4	<1
Sn-Beta-nano[a]	80	31	29	5
[Sn]-Beta-HF[a]	95	30	33	4

Conditions: 100 °C, 40 mg cat, 6 h, 2.5 mL of 125 mM glucose in H_2O. [a] Reaction time = 2 h.

to 45% were obtained, which are notably higher than those for Sn-MOR-bulk (20–33%) and [Sn]-Beta-HF (30–41%). Nanostructuring zeolites did not improve the catalytic performance for most zeolite topologies, except for the MWW zeolite.

Among the different sugar substrates, fructose was generally most efficiently converted to ML. For instance, the ML yield from fructose was 43% for Sn-MFI-bulk, whereas the conversion of glucose and sucrose yielded about half of this amount of ML. The highly crystalline hydrothermally synthesized [Sn]-MFI-bulk-F was equally active for fructose conversion (45% ML yield), and it could also efficiently convert glucose and sucrose to ML (29% and 43%, respectively). In this case, an increase of the reaction time to 64 h led to ML yields of 42%, 64% and 58% for glucose, fructose and sucrose, respectively. Similar yields for fructose conversion were reported by Davis and coworkers using Sn-MFI.[61] Only modest yields in the range of 18–33% could be obtained with Sn-MOR-bulk and Sn-Beta-nano.

The trends for the isomerization of glucose to fructose and the retro-aldolization of hexoses to methyl lactate are very different. One expects that Beta and MOR zeolites allow better accessibility for bulky hexose molecules to active Sn centers than MWW and MFI zeolites. This explains the

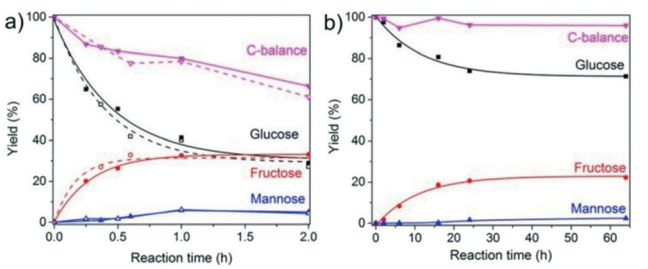

Fig. 7 The evolution of the composition of the reaction mixtures with time for glucose isomerization over a) Sn-Beta and b) Sn-MOR-bulk. Conditions: a) 2.5 mL of 125 mM glucose in water, 100 °C; b) 2.5 mL of 125 mM glucose in water, 100 °C, 40 mg cat. Dashed lines, open symbols (a): Sn-Beta-nano, solid lines, closed symbols: [Sn]-Beta-HF.

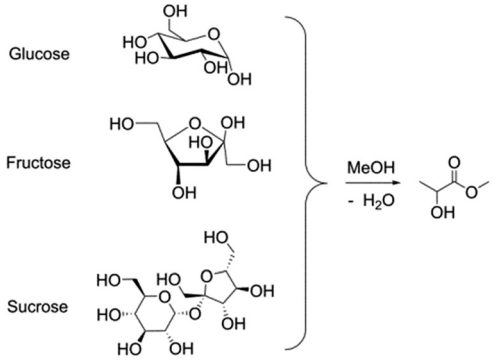

Scheme 3 Retro-aldol condensation of glucose, fructose and sucrose to methyl lactate.

difference in catalytic performance towards the glucose isomerization reaction under mild conditions (water, 100 °C). However, it cannot explain the different trends observed in retro-aldolization of sugars at higher temperature. Although the MWW and MFI zeolites were nearly inactive in glucose-to-fructose isomerization, they were the most active in the retro-aldolization of carbohydrates. Our results also show that the performance for retro-aldolization cannot be improved when the transport properties are enhanced by hierarchical structuring. A possible explanation for this difference is the stronger adsorption of carbohydrates in the smaller pores of MFI and MWW zeolites,[32] which increases the pore occupancy. The higher-temperature conditions of the retro-aldolization process remediate these adverse effects of the strong sugar adsorption in the narrow pores resulting in the high activity of Sn-MFI and Sn-MWW catalyst families. This would imply that catalytic activity is determined by adsorption and diffusion rather than intrinsic activity, which is not at odds with the observation that the activity does not correlate well with Sn content. It should also be considered that the rather bulky pyranose and furanose rings may experience difficulties in entering the pores of 10-membered ring zeolites, suggesting that the conversion of carbohydrates in the micropores may start with the acyclic forms. DFT calculations (Gaussian 09,[62] B3LYP/6-31+g(d,p), polarized continuum model for implicit water and methanol solvents) show that significantly more glucose (4–5%) is in the acyclic form at 160 °C compared to 100 °C (0.8–0.9%) and room temperature (0.05%). The better performance of Sn-MFI and Sn-MWW at high temperature may therefore be also at least partially attributed to the increased adsorption of the acyclic sugar and shape-selective conversion in the micropores. A more detailed mechanistic analysis is necessary to comprehensively rationalize all observed activity trends.

Table 6 Retro-aldolization of glucose, fructose and sucrose

		Methyl lactate yield from (%)		
Catalyst	Si/Sn	Glucose	Fructose	Sucrose
Sn-MWW-bulk	65	19	20	19
Sn-MWW-nano	73	36	40	28
Sn-MWW-delam	32	30	43	40
Sn-MFI-bulk	270	21	43	22
Sn-MFI-meso	97	15	31	32
Sn-MFI-nano	88	23	29	29
Sn-MFI-NS	67	31	44	43
[Sn]-MFI-bulk-F	109	29	45	43
Sn-MOR-bulk	33	20	33	27
Sn-MOR-nano	57	14	24	18
Sn-Beta-nano	80	21	18	23
[Sn]-Beta-HF[a]	95	30	41	40
Blank	—	7	3	2

Conditions: 160 °C, methanol, 112 mg sugar, 80 mg catalyst, 20 h. [a] 16 h.

4. Conclusions

Post-synthetic Sn functionalization of bulk and nanostructured zeolite catalysts involving stepwise dealumination and Sn grafting under anhydrous conditions was carried out to prepare Sn-modified MOR, MFI, MWW and Beta zeolites. The overall efficiency of the lattice Sn modification depends strongly on the stability and accessibility of the framework Al in the parent zeolite. Introducing mesopores in such zeolite crystals allows the increase of the attainable Sn loading in the modified catalysts. For 12MR zeolites Beta and MOR, this procedure is shown to be highly efficient irrespective of whether mesopores were present.

The catalytic properties of these Sn-modified zeolites were assessed by studying their performance in different model sugar conversion reactions, namely, the conversion of DHA to methyl lactate, the isomerization of glucose and the retro-aldolization of hexoses (glucose, fructose and sucrose). In line with our earlier proposals,[63] the presented results emphasize the role of the confinement effects on the intrinsic chemistry of the intrazeolite Sn sites for the overall catalytic performance in the liquid phase sugar conversion.

The activity trends varied substantially depending on the reactant. Whilst 12MR Sn-MOR and Sn-BEA zeolites were active in glucose-to-fructose isomerization, medium-pore 10MR zeolites hardly converted glucose under the relatively mild conditions employed for isomerization. We ascribe this effect to the strong confinement of the carbohydrate substrate inside the narrower MFI and MWW pores.

In line with this proposal, shortening of the diffusion paths by introducing mesopores did not improve the catalytic properties in glucose-to-fructose isomerization. The increase of the reaction temperature required to achieve retro-aldolization of hexoses remediates the adverse effect of the strong substrate adsorption. As a result, Sn-MFI and Sn-MWW zeolites produced high methyl lactate yields from different hexoses in methanol, in comparable quantities to the benchmark Sn-Beta zeolite. Although Sn-MOR showed some activity in the various test reactions, its performance was substantially lower compared to that of Sn-Beta, most likely due to the limited accessibility of the reactive lattice Sn sites inside the one-dimensional pore system of MOR zeolites and their substantially different nature as suggested by the results of the FTIR spectroscopy of adsorption probes.

The establishment of the molecular-level relationships between the structural and catalytic properties of Sn-modified materials requires additional dedicated and detailed studies combining advanced characterization[64–66] and thorough kinetic and *operando* studies[67] complemented by computations on realistic chemical models[68,69] accounting for the complexity of Sn-zeolite sugar conversion catalyst systems.

Acknowledgements

We thank Jan J. Wiesfeld for his help with FTIR spectroscopic characterization of the materials. This work was carried out in the framework of the CatchBio programme and the Joint Scientific Thematic Research Programme funded by the Netherlands Organization for Scientific Research (NWO) and the Chinese Ministry of Science and Technology. E. A. P. thanks the Ministry of Education and Science of the Russian Federation for support of his personal ITMO professorship (Project 11.1706.2017/4.6).

Notes and references

1 A. A. Rosatella, S. P. Simeonov, R. F. M. Frade and C. A. M. Afonso, *Green Chem.*, 2011, **13**, 754–793.
2 M. Dusselier, P. Van Wouwe, A. Dewaele, E. Makshina and B. F. Sels, *Energy Environ. Sci.*, 2013, **6**(2013), 1415–1442.
3 E. Nikolla, Y. Román-Leshkov, M. Moliner and M. E. Davis, *ACS Catal.*, 2011, **1**, 408–410.
4 M. S. Holm, Y. J. Pagán-Torres, S. Saravanamurugan, A. Riisager, J. A. Dumesic and E. Taarning, *Green Chem.*, 2012, **14**, 702–706.
5 S. Caratzoulas, M. E. Davis, R. J. Gorte, R. Gounder, R. F. Lobo, V. Nikolakis, S. I. Sandler, M. A. Snyder, M. Tsapatsis and D. G. Vlachos, *J. Phys. Chem. C*, 2012, **118**, 22815–22833.
6 I. Delidovich and R. Palkovits, *ChemSusChem*, 2016, **9**, 547–561.
7 P. Y. Dapsens, C. Mondelli and J. Perez-Ramirez, *Chem. Soc. Rev.*, 2015, **44**, 7025–7043.
8 T. Ennaert, J. Van Aelst, J. Dijkmans, R. De Clercq, W. Schutyser, M. Dusselier, D. Verboekend and B. F. Sels, *Chem. Soc. Rev.*, 2016, **45**, 584–611.
9 M. Moliner, Y. Roman-Leshkov and M. E. Davis, *Proc. Natl. Acad. Sci. U. S. A.*, 2010, **107**, 6164–6168.
10 L. Ren, Q. Guo, P. Kumar, M. Orazov, D. Xu, S. M. Alhassan, K. A. Mkhoyan, M. E. Davis and M. Tsapatsis, *Angew. Chem., Int. Ed.*, 2015, **54**, 10848–10851.
11 Q. Guo, F. Fan, E. A. Pidko, W. N. P. van der Graaff, Z. Feng, C. Li and E. J. M. Hensen, *ChemSusChem*, 2013, **6**, 1352–1356.
12 P. Y. Dapsens, C. Mondelli, J. Jagielski, R. Hauert and J. Pérez-Ramírez, *Catal. Sci. Technol.*, 2014, **4**, 2302–2311.
13 H. J. Cho, P. Dornath and W. Fan, *ACS Catal.*, 2014, **4**, 2029–2037.
14 C. M. Lew, N. Rajabbeigi and M. Tsapatsis, *Microporous Mesoporous Mater.*, 2012, **153**, 55–58.
15 F. de Clippel, M. Dusselier, R. Van Rompaey, P. Vanelderen, J. Dijkmans, E. Makshina, L. Giebeler, S. Oswald, G. V. Baron, J. F. Denayer, P. P. Pescarmona, P. A. Jacobs and B. F. Sels, *J. Am. Chem. Soc.*, 2012, **134**, 10089–10101.
16 L. Li, C. Stroobants, K. Lin, P. A. Jacobs, B. F. Sels and P. P. Pescarmona, *Green Chem.*, 2011, **13**, 1175–1181.
17 C. M. Osmundsen, M. S. Holm, S. Dahl and E. Taarning, *Proc. R. Soc. A*, 2012, **468**, 2000–2016.
18 C. Hammond, D. Padovan, A. Al-Nayili, P. P. Wells, E. K. Gibson and N. Dimitratos, *ChemCatChem*, 2015, **7**, 3322–3331.
19 C. Hammond, S. Conrad and I. Hermans, *Angew. Chem., Int. Ed.*, 2012, **51**, 11736–11739.
20 W. N. P. van der Graaff, G. Li, B. Mezari, E. A. Pidko and E. J. M. Hensen, *ChemCatChem*, 2015, **7**, 1152–1160.
21 P. Wolf, M. Valla, A. J. Rossini, A. Comas-Vives, F. Núñez-Zarur, B. Malaman, A. Lesage, L. Emsley, C. Copéret and I. Hermans, *Angew. Chem., Int. Ed.*, 2014, **53**, 10179–10183.
22 Y. G. Kolyagin, A. V. Yakimov, S. Tolborg, P. N. R. Vennestrom and I. I. Ivanova, *J. Phys. Chem. Lett.*, 2016, **7**, 1249–1253.
23 P. Wolf, W.-C. Liao, T.-C. Ong, M. Valla, J. W. Harris, R. Gounder, W. N. P. van der Graaff, E. A. Pidko, E. J. M. Hensen, P. Ferrini, J. Dijkmans, B. Sels, I. Hermans and C. Copéret, *Helv. Chim. Acta*, 2016, **99**, 916–927.
24 W. R. Gunther, V. K. Michaelis, M. A. Caporini, R. G. Griffin and Y. Román-Leshkov, *J. Am. Chem. Soc.*, 2014, **136**, 6219–6222.
25 S. Roy, K. Bakhmutsky, E. Mahmoud, R. F. Lobo and R. J. Gorte, *ACS Catal.*, 2013, **3**, 573–580.
26 M. Boronat, P. Concepción, A. Corma, M. Renz and S. Valencia, *J. Catal.*, 2005, **234**, 111–118.
27 R. Bermejo-Deval, M. Orazov, R. Gounder, S.-J. Hwang and M. E. Davis, *ACS Catal.*, 2014, **4**, 2288–2297.
28 J. W. Harris, M. J. Cordon, J. R. Di Iorio, J. C. Vega-Vila, F. H. Ribeiro and R. Gounder, *J. Catal.*, 2016, **335**, 141–154.
29 V. Choudhary, S. Caratzoulas and D. G. Vlachos, *Carbohydr. Res.*, 2013, **368**, 89–95.
30 N. Rai, S. Caratzoulas and D. G. Vlachos, *ACS Catal.*, 2013, **3**, 2294–2298.
31 G. Yang, E. A. Pidko and E. J. M. Hensen, *J. Phys. Chem. C*, 2013, **117**, 3976–3986.
32 G. Li, E. A. Pidko and E. J. M. Hensen, *Catal. Sci. Technol.*, 2014, **4**, 2241–2250.
33 Y.-P. Li, M. Head-Gordon and A. T. Bell, *ACS Catal.*, 2014, **4**, 1537–1545.
34 G. Li, E. A. Pidko and E. J. M. Hensen, *ACS Catal.*, 2016, **6**, 4162–4169.
35 E. Taarning, S. Saravanamurugan, M. S. Holm, J. Xiong, R. M. West and C. H. Christensen, *ChemSusChem*, 2009, **2**, 625–627.
36 M. S. Holm, S. Saravanamurugan and E. Taarning, *Science*, 2010, **328**, 602–605.
37 R. Bermejo-Deval, R. Gounder and M. E. Davis, *ACS Catal.*, 2012, **2**, 2705–2713.
38 J. Pérez-Ramírez, C. H. Christensen, K. Egeblad, C. H. Christensen and J. C. Groen, *Chem. Soc. Rev.*, 2008, **37**, 2530–2542.
39 J. Jin, X. Ye, Y. Li, Y. Wang, L. Li, J. Gu, W. Zhao and J. Shi, *Dalton Trans.*, 2014, **43**, 8196–8204.

40 A. Al-Nayili, K. Yakabi and C. Hammond, *J. Mater. Chem. A*, 2016, **4**, 1373–1382.
41 R. De Clercq, M. Dusselier, C. Christiaens, J. Dijkmans, R. I. Iacobescu, Y. Pontikes and B. F. Sels, *ACS Catal.*, 2015, **5**, 5803–5811.
42 A. Corma, M. E. Domine and S. Valencia, *J. Catal.*, 2003, **215**, 294–304.
43 A. Corma, L. T. Nemeth, M. Renz and S. Valencia, *Nature*, 2001, **412**, 423–425.
44 T. Iida, A. Takagaki, S. Kohara, T. Okubo and T. Wakihara, *ChemNanoMat*, 2015, **1**, 155–158.
45 Z. Kang, X. Zhang, H. Liu, J. Qiu, W. Han and K. L. Yeung, *Mater. Chem. Phys.*, 2013, **141**, 519–529.
46 P. Li, G. Liu, H. Wu, Y. Liu, J.-G. Jiang and P. Wu, *J. Phys. Chem. C*, 2011, **115**, 3663–3670.
47 M. Liu, S. Jia, C. Li, A. Zhang, C. Song and X. Guo, *Chin. J. Catal.*, 2014, **35**, 723–732.
48 P. Wolf, C. Hammond, S. Conrad and I. Hermans, *Dalton Trans.*, 2014, **43**, 4514–4519.
49 B. Tang, W. Dai, G. Wu, N. Guan, L. Li and M. Hunger, *ACS Catal.*, 2014, **4**, 2801–2810.
50 J. Dijkmans, M. Dusselier, D. Gabriëls, K. Houthoofd, P. C. M. M. Magusin, S. Huang, Y. Pontikes, M. Trekels, A. Vantomme, L. Giebeler, S. Oswald and B. F. Sels, *ACS Catal.*, 2015, **5**, 928–940.
51 J. Dijkmans, D. Gabriëls, M. Dusselier, F. de Clippel, P. Vanelderen, K. Houthoofd, A. Malfliet, Y. Pontikes and B. F. Sels, *Green Chem.*, 2013, **15**, 2777–2785.
52 C. H. L. Tempelman, V. O. de Rodrigues, E. R. H. van Eck, P. C. M. M. Magusin and E. J. M. Hensen, *Microporous Mesoporous Mater.*, 2015, **203**, 259–273.
53 D. P. Serrano, J. Aguado, J. M. Escola, J. M. Rodríguez and Á. Peral, *Chem. Mater.*, 2006, **18**, 2462–2464.
54 X. Zhu, L. Wu, P. C. M. M. Magusin, B. Mezari and E. J. M. Hensen, *J. Catal.*, 2015, **327**, 10–21.
55 C. H. L. Tempelman, M. T. Portilla, M. E. Martínez-Armero, B. Mezari, N. G. R. de Caluwé, C. Martínez and E. J. M. Hensen, *Microporous Mesoporous Mater.*, 2016, **220**, 28–38.
56 A. Corma, U. Diaz, V. Fornés, J. M. Guil, J. Martínez-Triguero and E. J. Creyghton, *J. Catal.*, 2000, **191**, 218–224.
57 S. Tolborg, A. Katerinopoulou, D. D. Falcone, I. Sádaba, C. M. Osmundsen, R. J. Davis, E. Taarning, P. Fristrup and M. S. Holm, *J. Mater. Chem. A*, 2014, **2**, 20252–20262.
58 J. C. Groen, S. Abelló, L. A. Villaescusa and J. Pérez-Ramírez, Mesoporous beta zeolite obtained by desilication, *Microporous Mesoporous Mater.*, 2008, **114**, 93–102.
59 J. Datka, A. M. Turek, J. M. Jehng and I. E. Wachs, *J. Catal.*, 1992, **135**, 186–199.
60 Y. B. Tewari, *Appl. Biochem. Biotechnol.*, 1990, **23**, 187–203.
61 M. Orazov and M. E. Davis, *Proc. Natl. Acad. Sci. U. S. A.*, 2015, **112**, 11777–11782.
62 M. J. Frisch, G. W. Trucks, H. B. Schlegel, G. E. Scuseria, M. A. Robb, J. R. Cheeseman, G. Scalmani, V. Barone, B. Mennucci, G. A. Petersson, H. Nakatsuji, M. Caricato, X. Li, H. P. Hratchian, A. F. Izmaylov, J. Bloino, G. Zheng, J. L. Sonnenberg, M. Hada, M. Ehara, K. Toyota, R. Fukuda, J. Hasegawa, M. Ishida, T. Nakajima, Y. Honda, O. Kitao, H. Nakai, T. Vreven, J. A. Montgomery Jr., J. E. Peralta, F. Ogliaro, M. J. Bearpark, J. Heyd, E. N. Brothers, K. N. Kudin, V. N. Staroverov, R. Kobayashi, J. Normand, K. Raghavachari, A. P. Rendell, J. C. Burant, S. S. Iyengar, J. Tomasi, M. Cossi, N. Rega, N. J. Millam, M. Klene, J. E. Knox, J. B. Cross, V. Bakken, C. Adamo, J. Jaramillo, R. Gomperts, R. E. Stratmann, O. Yazyev, A. J. Austin, R. Cammi, C. Pomelli, J. W. Ochterski, R. L. Martin, K. Morokuma, V. G. Zakrzewski, G. A. Voth, P. Salvador, J. J. Dannenberg, S. Dapprich, A. D. Daniels, Ö. Farkas, J. B. Foresman, J. V. Ortiz, J. Cioslowski and D. J. Fox, *Gaussian 09*, in, Gaussian, Inc., Wallingford, CT, USA, 2009.
63 W. N. P. van der Graaff, C. H. L. Tempelman, G. Li, B. Mezari, N. A. Kosinov, E. A. Pidko and E. J. M. Hensen, *ChemSusChem*, 2016, **9**, 3145–3149.
64 T. Kobayashi, F. A. Perras, I. I. Slowing, A. D. Sadow and M. Pruski, *ACS Catal.*, 2015, **5**, 7055–7062.
65 W. R. Gunther, V. K. Michaelis, R. G. Griffin and Y. Román-Leshkov, *J. Phys. Chem. C*, 2016, **120**, 28533–28544.
66 A. V. Yakimov, Y. G. Kolyagin, S. Tolborg, P. N. R. Vennestrøm and I. I. Ivanova, *J. Phys. Chem. C*, 2016, **120**, 28083–28092.
67 L. Q. R. Alamillo, W. A. Elliott, A. Andersen, D. W. Hoyt, E. D. Walter, K. S. Han, N. M. Washton, R. M. Rioux, J. A. Dumesic and S. L. Scott, *ACS Catal.*, 2017, **7**, 3489–3500.
68 E. A. Pidko, *ACS Catal.*, 2017, **7**, 4230–4234.
69 H. A. Doan, M. K. Sharma, W. S. Epling and L. C. Grabow, *ChemCatChem*, 2017, **9**, 1594–1600.

